The Plateau-Rayleigh instability in solids is a simple phase separation

Chen Xuan and John Biggins
Cavendish Laboratory, University of Cambridge, 19 JJ Thomson Avenue, Cambridge CB3 0HE, United Kingdom
(Dated: April 6, 2017)

A long elastic cylinder, radius a and shear-modulus μ, becomes unstable given sufficient surface tension γ. We show this instability can be simply understood by considering the energy, $E(\lambda)$, of such a cylinder subject to a homogenous longitudinal stretch λ. Although $E(\lambda)$ has a unique minimum, if surface tension is sufficient ($\Gamma \equiv \gamma/(a\mu) > \sqrt{32}$) it looses convexity in a finite region. We use a Maxwell construction to show that, if stretched into this region, the cylinder will phase separate into two segments with different stretches λ_1 and λ_2. Our model thus explains why the instability has infinite wavelength, and allows us to calculate the instability's sub-critical hysteresis loop (as a function of imposed stretch), showing that instability proceeds with constant amplitude and at constant (positive) tension as the cylinder is stretched between λ_1 and λ_2. We use full nonlinear finite-element calculations to verify these predictions, and to characterize the interface between the two phases. Near $\Gamma = \sqrt{32}$ the length of such an interface diverges introducing a new length-scale and allowing us to construct a 1-D effective theory. This treatment yields an analytic expression for the interface itself, revealing its characteristic length grows as $l_{wall} \sim a/\sqrt{\Gamma - \sqrt{32}}$.

Molecules at a condensed phase's surface have fewer neighbors than those in the bulk, so all materials suffer an energy proportional to their exposed area. The resulting tendency to reduce area is familiar in fluids, explaining why droplets are round, taps drip and pond-skaters don't drown. An isolated fluid body always form a sphere under surface tension, but the corresponding problem for a solid body is altogether more subtle, pitting surface tension against bulk elasticity. Here we give a full account of this competition in long solid cylinders.

In general a surface energy, γ, can only compete with a bulk elastic shear-modulus, μ, at scales below the elastocapiliary length, $l_{cap} = \gamma/\mu$, which is sub-Angtrom in crystalline materials but reaches up to microns or even millimeters in soft solids such as gels and biological tissues. Elastocapillary distortions [1] thus occur in the realm of the small and soft, including microfluidics [2], the processing of polymer strands [3, 4] and many aspects of biology [5–8]. In addition to the deformations of soft cylinders considered here [9–15], recent work has highlighted capillarity-driven bending of wet elastic rods and sheets [16–19], elastic modifications to wetting [20–22], and the inhibitory role of surface tension in elastic creasing [23–25] and cavitation [26].

In fluid cylinders, surface tension famously causes disintegration into spherical droplets [27]. The driver for this *Plateau-Rayleigh instability* is that an undulation along a cylinder reduces its surface area if its wavelength is longer than its circumference. How the instability proceeds depends in on the fluid [28, 29], but this simple geometric origin means, inescapably, that all fluid cylinders ultimately disintegrate. A solid cylinder (radius a) is also subject to the same geometric reality, but in this case, the surface energy saved by undulation only outweighs the elastic cost of deforming the cylinder if $l_{cap} \gtrsim a$ [10], so only thin soft cylinders are unstable. Solid cylinders cannot break into spheres, so the instability produces stable undulating cylinders, fig. 1, with a *beads-on-a-string* morphology emerging at high surface tension. Previous

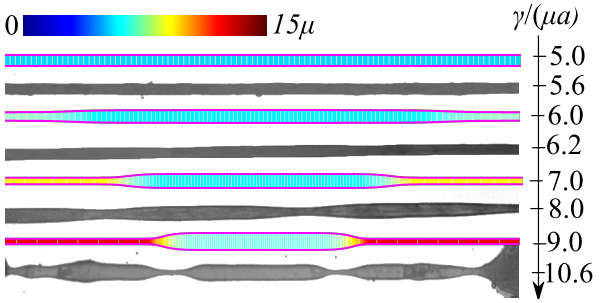

FIG. 1. Equilibrium shapes of agar-gel [11] and finite-element cylinders (radius a, shear-modulus μ) ordered by their elastocapiliary number $\Gamma = \gamma/(\mu a)$ and showing Plateau-Rayleigh instability for $\Gamma \gtrsim 6$. The finite element instability adopts the longest possible wavelength, and is colored by pressure.

groups have observed this instability [9, 11] and studied its onset via linear stability theory [10, 11], showing the first unstable mode has infinite wavelength. More recent work has focussed on stretched cylinders [12–14], showing, with linear stability theory, that the instability occurs in a particular stretch-interval, $\lambda_1 < \lambda < \lambda_2$, and, via finite element numerics, that, between λ_1 and λ_2, the bead amplitude is essentially constant while bead length falls [14]. Here we demonstrate that this long-wavelength constant-amplitude beading arises because the instability is actually a longitudinal phase separation between a less and a more stretched phase. We are able to simply predict the instability's full high-amplitude behavior, including its hysteresis loop, verify our predictions with finite elements, and identify and analyze the domain walls separating the two phases.

We consider a long elastic cylinder, radius a and length L, that undergoes a displacement $\mathbf{u}$ and consequent deformation gradient $F = I + \nabla\mathbf{u}$. We model the cylinder as incompressible and neo-Hookean with shear-modulus

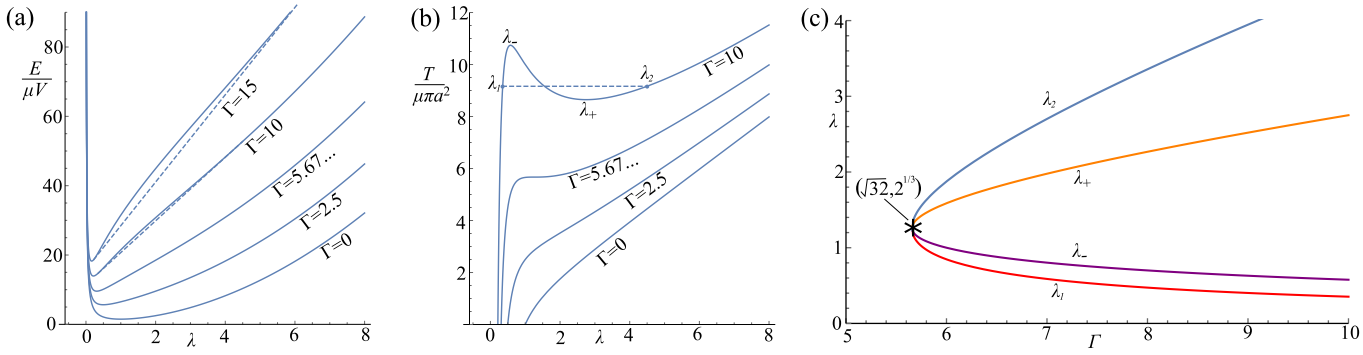

FIG. 2. Energy (a) and tension (its derivative, b) of an elastic cylinder stretched by λ at various elastocapiliary numbers Γ. As Γ increases the minimum-energy/zero-tension stretch moves below one and, for $\Gamma > \sqrt{32} = 5.67..$, a region of negative curvature appears in the energy between λ_- and λ_+, corresponding to an unstable region where tension falls with extension. In (a) the dashed line indicates the energy's common-tangent chord, which spans the concave region meeting the energy at $\lambda_1 < \lambda_-$ and $\lambda_2 > \lambda_+$. The cylinder can pay the lower common-tangent energy by phase-separating into λ_1 and λ_2 regions and (dashed line in b) thus stretches from λ_1 to λ_2 at constant tension. Fig (c) plots the stretch ratios λ_1, λ_2 and $\lambda_\pm$ as a function of Γ.

μ and surface energy γ, so the cylinder's total energy is

$$E = \gamma A + \int \frac{1}{2}\mu \left[\text{ Tr}\left(F \cdot F^T\right)\right] dV, \tag{1}$$

where A is the cylinder's external area, and incompressibility requires $\text{Det}(F) = 1$. Previous studies have shown this energy first becomes linearly-unstable to an infinite wavelength perturbation when $\gamma = 6\mu a$ [10, 11]. We first verify that long-wavelength behavior persists far beyond threshold by conducting full finite element calculations at $\gamma = 8\mu a$ in long aspect ratio cylinders ($L = 100a$, see appendix B) and observe that, although instability arises with a finite wavelength, it coarsens (movie S1), saving energy, until, as seen in fig. 1, the longest possible mode is reached. To understand this, we imagine stretching the cylinder homogeneously to a length λL, causing a contraction of its radius to $a/\sqrt{\lambda}$ so that the volume, $V = \pi a^2 L$, is preserved. The cylinder's surface area thus increases to $2\pi a L\sqrt{\lambda}$, and its deformation gradient is $F = \text{diag}(1/\sqrt{\lambda}, 1/\sqrt{\lambda}, \lambda)$, so its total energy is

$$E(\lambda) = \pi\mu L a^2 \left(2\Gamma\sqrt{\lambda} + \frac{1}{2}\left(\lambda^2 + \frac{2}{\lambda}\right)\right), \tag{2}$$

where we have introduced $\Gamma = \gamma/(\mu a) = l_{cap}/a$, the elastocapillary number for the cylinder. We plot $E(\lambda)$ for several values of Γ in fig. 2a. The elastic part of the energy is a convex function minimized at $\lambda = 1$. The surface energy never dominates at small or large λ, and the the total energy always has a single minimum, though it moves to $\lambda < 1$ as Γ increases [19]. However, the surface tension term, proportional to $\sqrt{\lambda}$, is a concave function and, when Γ is sufficient, it introduces a concave region into the total energy. This concave region ($\frac{d^2E}{d\lambda^2} < 0$) is mechanically unstable since therein the extensive force required (or total tension),

$$T = \frac{1}{L}\frac{dE}{d\lambda} = \pi\mu a^2\left(\frac{\Gamma}{\sqrt{\lambda}} + \lambda - \frac{1}{\lambda^2}\right), \tag{3}$$

falls with increasing stretch, as seen in fig. 2b. The limits of this mechanically unstable region are

$$\lambda_\pm = \left[\frac{1}{4}\left(\Gamma \pm \sqrt{\Gamma^2 - 32}\right)\right]^{2/3}, \tag{4}$$

where $\frac{d^2E}{d\lambda^2} = 0$. The concave region arises when $\Gamma > \sqrt{32}$, first appearing at $\lambda\pm = 2^{1/3}$ and spreading out reaching $\lambda_- = 1$ at $\Gamma = 6$, both in agreement with previous linear stability thresholds [11, 13]. In general, given a pair of stretch ratios, λ_1 and λ_2, the cylinder can achieve on average any intermediate stretch $\lambda_1 < \lambda < \lambda_2$ by phase separating into a λ_1 region and a λ_2 region with appropiate length fractions, at an energy cost that corresponds to the chord connecting $E(\lambda_1)$ and $E(\lambda_2)$. In the concave region such chords lie below the original energy, so phase-separation saves energy. As understood by Maxwell [30], the optimal phase-separation arises when the chord is tangent to the energy at both λ_1 and λ_2:

$$E'(\lambda_1) = E'(\lambda_2) \tag{5}$$

$$E(\lambda_1) + E'(\lambda_1)(\lambda_2 - \lambda_1) = E(\lambda_2). \tag{6}$$

The solutions for λ_1 and λ_2 as functions of Γ are shown in fig. 2c. As the cylinder is stretched from λ_1 to λ_2, it lowers its energy by phase separating onto the common tangent line, shown as a dashed line in fig. 2a, stretching from λ_1 to λ_2 by adjusting the length-fraction of the two phases. Since the resulting effective energy is a straight line, the *tension is constant during the transition* as shown by the dotted line in fig. 2b. Furthermore, an obvious conclusion of this phase separation approach is that *no amount of surface tension will destabilize a*

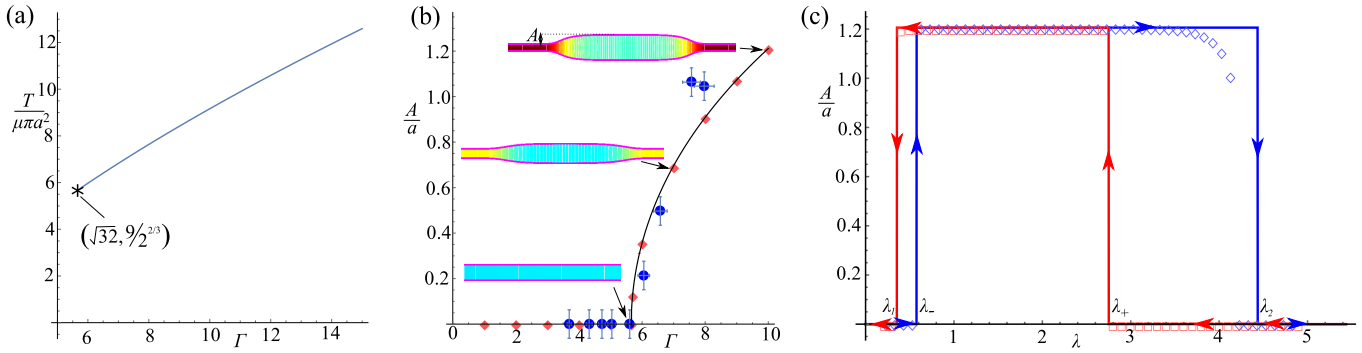

FIG. 3. Tension (a) and amplitude (b) of surface-tension driven phase-separation in an elastic cylinder as a function of elastocapiliary number Γ. In (b) we compare theory (solid line), finite elements (red diamonds) and experimental data (blue circles) from [11]. (c): Comparison of theoretical (solid lines) and finite element (points) hysteresis loops showing amplitude as a function of imposed stretch at $\Gamma = 10$; the constant amplitude is the hallmark of phase separation.

solid cylinder unless it is also stretched to the transition tension $T = (1/L)E'(\lambda_1)$, plotted in fig. 3a. Following the common-tangent yields a convex effective energy, so there is no additional instability.

When it is phase-separated, the difference in final radius between the λ_1 segment (the "bead") and the λ_2 segment (the "string") is simply

$$A = \frac{a}{\sqrt{\lambda_1}} - \frac{a}{\sqrt{\lambda_2}}. \tag{7}$$

This *amplitude does not change as the cylinder is stretched* from λ_1 to λ_2. Such constant amplitude beading between two stretch ratios, (movie S2), has been observed without explanation in rat sciatic nerve [31] and elasto-capiliary finite elements [14]. We compare experimental amplitudes with our finite-element and phase-separation amplitudes in fig. 3b. The three agree well, with finite elements exactly reproducing the phase-separation amplitudes, verifying our approach.

If instability were produced by increasing Γ it would be continuous (supercritical) but if it is controlled at fixed Γ by stretching from λ_1 to λ_2 it will be observed as a discontinuous (subcritical) with constant amplitude $A(\Gamma)$ throughout. In a stretching cycle the cylinder will be stretched from the energy minimizing contraction λ_{min} to λ_1 homogeneously. Upon passing λ_1 it would save energy by phase separating, but the cylinder nevertheless remains mechanically stable until it reaches the end of convexity, λ_-, only then phase separating into λ_1 and λ_2. As stretching continues further, the cylinder shifts material from the λ_1 phase to the λ_2 phase, causing bead width to fall at constant amplitude, until all the material is at λ_2, concluding the instability. Similarly in unloading, the instability should occur at λ_+, but then persist down to λ_1. We thus predict the sub-critical hysteresis loop for a stretch cycle shown in fig. 3c. Hysteresis also slightly complicates the tension-extension behavior: we expect the tension to remain on the homogeneous curve in loading until λ_- then drop to the phase separation value, and remain there until λ_2.

Our hysteresis predictions are compared with a finite element stretch-cycle in fig. 3c, showing good agreement with one discrepancy: the finite-element loading cycle amplitude drops off slightly early. The reason for this is made evident by plotting (fig. 4a) the longitudinal stretch ratio $\lambda(z)$ (on the axis of the cylinder) as a function of length along the cylinder, running from the middle of the bead ($z = 0$) to the end of the cylinder ($z = L/2$), for various values of the total imposed stretch $< \lambda >$ that traverse the instability. In these plots we see clearly that the cylinder has separated into λ_1 and λ_2 regions, but also that they are connected by a transition region—a *domain wall*—with finite length. The energy cost and length-fraction of a domain wall is negligible in an infinite cylinder, but matters in a finite one: upon stretching a finite cylinder towards λ_2 the amplitude drops early because the vanishing length of the λ_1 segment becomes comparable to the domain wall, so the domain-wall raises the phase-separation energy above the homogeneous energy. As expected, in longer cylinders, the instability persists closer to λ_2. In contrast, at the onset of instability (λ_-) the energy minimizing configuration already requires an extensive length fraction of both phases, so instability proceeds even in modest length cylinders.

Around the critical point, $\Gamma = \sqrt{32}$ and $\lambda = 2^{1/3}$, we can solve the phase separation model analytically, and *model the domain wall*. Expanding (5-6) in $\epsilon = \Gamma - \sqrt{32}$, we see the leading order behavior of λ_1 and λ_2 is

$$\lambda_1 = 2^{1/3} - \frac{1}{\sqrt{3}} 2^{7/12}\sqrt{\epsilon}, \quad \lambda_2 = 2^{1/3} + \frac{1}{\sqrt{3}} 2^{7/12}\sqrt{\epsilon}, \tag{8}$$

and hence the amplitude and tension are

$$A = a\frac{1}{\sqrt{3}} \sqrt[12]{2}\sqrt{\epsilon}, \qquad T = \frac{\pi\mu a^2}{2^{2/3}}\left(\sqrt{2}\epsilon + 9\right). \tag{9}$$

To model the domain wall we require an energy that penalizes stretch gradients along the cylinder. Such a

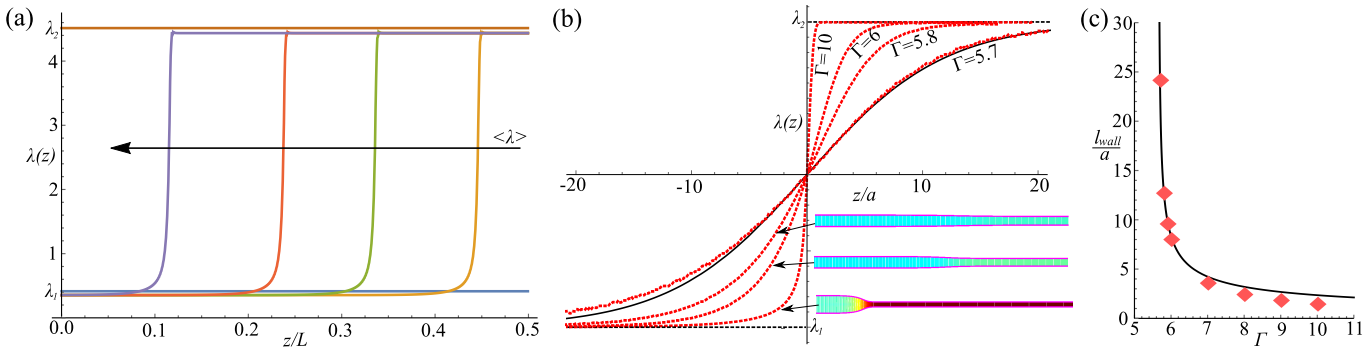

FIG. 4. Domain walls between separated phases. (a) Finite element calculation of stretch ratio $\lambda(z)$ along a $\Gamma = 10$ cylinder during phase separation, showing a λ_1 and λ_2 regions separated by a domain wall that moves along the cylinder as the average stretch, $\langle\lambda\rangle$, is increased. (b) Finite element domain walls (red dots) in cylinders at various elastocapiliary numbers Γ. The domain walls spreads out and becomes more symmetric as $\Gamma \to \sqrt{32}$, agreeing with the black theoretical curve (eqn. (14)) by $\Gamma = 5.7$. (c) Comparison of theory (curve) and finite-elements (points) for the domain wall length, l_{wall}, as a function of Γ.

term could arise from additional elastic shear or additional surface area. We capture both effects by allowing the longitudinal stretch, $\lambda(z)$, to vary slowly along the cylinder's length so a point initially at (r, z) is moved to $(r/\sqrt{\lambda(z)}, \int \lambda(z)dz)$. This introduces a new shear term into the deformation gradient, $F_{rz} = -r\lambda'/(2\lambda^{3/2})$, increasing the elastic energy per unit-length to

$$E_{el} = \frac{1}{2}\mu\left(\frac{2}{\lambda^2} + \lambda^2 + \frac{a^2\lambda'^2}{16\lambda^3}\right)\pi a^2 \tag{10}$$

and the surface energy per-unit length to

$$E_s = \gamma\frac{2\pi a}{\sqrt{\lambda}}\sqrt{\lambda^2 + \frac{a^2\lambda'^2}{4\lambda^3}}. \tag{11}$$

Finally, we use T as a Lagrange multiplier constraining the average stretch to $\langle\lambda\rangle$, leading us to the total energy

$$E = \int E_s + E_{el} - T(\lambda - \langle\lambda\rangle)dz. \tag{12}$$

Near the critical point we can take the above form for T and write $\lambda = 2^{1/3} + \frac{1}{\sqrt{3}}2^{7/12}\sqrt{\epsilon}h(z)$, where $h(z)$ varies between ± 1 through a domain wall. Expanding in ϵ and keeping only the lowest order terms h' and h terms yields

$$E = \int \text{const} + \frac{17\pi a^4\mu\epsilon h'^2}{24\ 2^{5/6}} + \frac{\pi a^2\mu\epsilon^2}{12\sqrt[3]{2}}h^2\left(h^2 - 2\right)dz, \tag{13}$$

where the ϵ^2 term is minimized by $h = \pm 1$, while the ϵ term penalizes gradients. Minimizing E w.r.t variations in h requires $17a^2h'' - 4\sqrt{2}\epsilon h\left(h^2 - 1\right) = 0$, and hence

$$h(z) = \tanh\left(\frac{2^{3/4}\sqrt{\epsilon}}{\sqrt{17}a}z\right), \tag{14}$$

an *explicit form for the domain-wall.* The walls are exponentially localized with a characteristic length $l_{wall} = 2 \times \sqrt{17}a/(2^{3/4}\sqrt{\epsilon})$ that diverges near the critical point. In fig. 4b we plot $\lambda(z)$ through finite-element domain walls at various Γ, showing very good agreement with eqn. (14) near $\Gamma = \sqrt{32}$. In fig. 4c we show the length of the finite element domain walls (defined as the z interval required for $\tanh(1) \approx 0.76$ of the λ variation) diverges near the critical point, in accord with our prediction. We emphasize that the instability is long-wavelength for all values of Γ beyond instability, meaning the energy minimum is a pair of phases separated by a single domain wall. In this calculation we have shown, in addition, that near the critical point the width of the domain wall itself diverges. Although this analysis captures the essential physics, it assumes z displacements are independent of r; relaxing this assumption leads to a small decrease in l_{wall} by a factor of $\sqrt{34/33}$ (see appendix A).

In summary, the solid Plateau-Rayleigh instability is a phase separation between regions of different but homogeneous longitudinal stretches connected by exponentially localized domain walls. This structure, reminiscent of elastic necking [32, 33], balloon instabilities [34, 35] and volume transitions in swelling gels [9, 36, 37], provides a picture of the instability that is both simple and complete. In general, a real elastic cylinder stretched by λ will be better described by a more sophisticated elastic energy $W(\lambda)$, where $W(\lambda)$ may include a Mooney-Rivlin [38, 39] term $(2\lambda + 1/\lambda^2)$, and/or strain-stiffening at large extension (Gent [40] and Arruda-Boyce [41] energies) to model the limit of extensibility of finite-length polymer chains. However, like the neo-Hookean energy, all of these elastomer/gel energies lead to a $W(\lambda)$ that is convex and minimized at $\lambda = 1$, reflecting the fact that elastomeric fibers do not spontaneously phase-separate (neck) in extension. In all these cases, adding a surface energy, $\Gamma\sqrt{\lambda}$, which is concave will, if Γ is sufficient, generate a concave region in the total energy, and hence cause phase separation in extension in the same manner, though with different critical stretches and threshold Γ.

In particular, in the more realistic strain-stiffening models, the stretch ratio in the stretched phases, λ_2, will be reduced to lie beneath the limit of extensibility, reducing the amplitude but not the nature of the instability, and ensuring the pair of stretch-ratios in phase-separation lie within the range attainable by the elastic cylinder in question. Similarly, since phase-separation originates solely in the non-convexity of surface energy, this picture will certainly generalize to Voigt viscoelasticity and more elaborate extruded prismatic shapes, and, since it naturally produces a high amplitude beads-on-a-string morphology, may underpin the more famous bead/string pattern formed during the breakup of viscoelastic threads [28]. Mastering these instabilities is essential for the better sculpting, spinning and processing of polymer fibers [3, 4]; we note that a very similar mechanism drives beading of nerves under tension [31], and speculate that evolution has already harnessed this instability to sculpt the insulating myelin sheath around axons into beads separated by Ranvier nodes [42] during neuronal development.

ACKNOWLEDGMENTS

Acknowledgements. We thank S. Mora for sharing data and images, and T. Tallinen, on whose code our finite element calculations are based. C.X. thanks the China Scholarship Council and the EPSRC for funding.

Appendix A: Exact expression for the domain wall close to the point of instability

To obtain an expression for the domain wall we undertake a small-gradient expansion of the fields in a long elastic cylinder subject to surface tension and close to its point of instability. We first consider a long elastic cylinder, of radius a and shear modulus μ, subject to a surface tension $\gamma = \Gamma\mu a$. The cylinder is aligned along the z axis of a cylindrical coordinate system and undergoes a uniaxial deformation that moves the material at (R, θ, Z) to $(r(R, Z), \theta, z(R, Z))$, leading to the (cylindrical-coordinate) deformation gradient

$$F = \begin{pmatrix} \frac{\partial r}{\partial R} & 0 & \frac{\partial r}{\partial Z} \\ 0 & r/R & 0 \\ \frac{\partial z}{\partial R} & 0 & \frac{\partial z}{\partial Z} \end{pmatrix}. \tag{A1}$$

As in the main text, if the cylinder is subject to a tension T, its mechanical behavior is given by the minimum of the effective energy

$$E = \int \mathcal{E}\, dZ = \int \left(E_s + E_{el} - T \frac{\partial z}{\partial Z}\bigg|_{R=0} \right) dZ, \tag{A2}$$

where the surface energy per unit length is

$$E_s = \Gamma a \mu 2\pi r(a, Z) \sqrt{\left(\frac{\partial r(a, Z)}{\partial Z}\right)^2 + \left(\frac{\partial z(a, Z)}{\partial Z}\right)^2}, \tag{A3}$$

but the elastic energy per unit length must now include a pressure-field Lagrange multiplier to enforce volume conservation throughout the cylinder

$$E_{el} = \int_0^a \frac{1}{2}\mu \left[\mathrm{Tr}\left(F \cdot F^T\right) + P(\mathrm{Det}\,(F) - 1) \right] 2\pi R \mathrm{d}R. \tag{A4}$$

Introducing the PK1 stress $\sigma = \mu F + \mathrm{Det}\,(F) F^{-T} P$, we see that minimizing E with respect to variations in r, z leads to the familiar equations of elastic equilibrium inside the cylinder

$$\nabla\cdot\sigma = 0 \quad \Longrightarrow \quad \begin{cases} \sigma_{rR,R} + \sigma_{rZ,Z} + (\sigma_{rR} - \sigma_{\theta\theta})/R = 0, \\ \sigma_{zR,R} + \sigma_{zZ,Z} + \sigma_{zR}/R = 0, \end{cases} \tag{A5}$$

and the boundary condition at the outer surface

$$\sigma \cdot (2\pi a \hat{\mathbf{r}}) = \begin{pmatrix} -\frac{\partial E_s}{\partial r} + \frac{d}{dZ}\frac{\partial E_s}{\partial r_{,Z}} \\ 0 \\ \frac{d}{dZ}\frac{\partial E_s}{\partial z_{,Z}} \end{pmatrix}, \tag{A6}$$

where, for conciseness, we use comma-notation for partial derivatives. Finally, minimizing E with respect to P yields the expected condition of incompressibility,

$$\mathrm{Det}\,(F) = 1. \tag{A7}$$

We know from the main text that instability first occurs at $\Gamma = \sqrt{32}$ in a homogeneously strained cylinder with $z = 2^{1/3}Z$ and $r = R/2^{1/6}$. Furthermore, just beyond the threshold for instability, $\Gamma = \sqrt{32}+\epsilon$, we expect variation in the Z direction only over length scales $a/\sqrt{\epsilon}$, and strains no larger than $\mathcal{O}(\sqrt{\epsilon})$, so we can write the pressure and position fields as expansions in $\sqrt{\epsilon}$,

$$z = 2^{1/3}Z + a z_0\left(\tilde{Z}\right) + \sum_{i=1}^{\infty} \epsilon^{i/2} a z_i\left(\tilde{R}, \tilde{Z}\right) \tag{A8}$$

$$r = \frac{R}{2^{1/6}} + \sum_{i=1}^{\infty} \epsilon^{i/2} a r_i\left(\tilde{R}, \tilde{Z}\right) \tag{A9}$$

$$P = \mu P_0 + \sum_{i=1}^{\infty} \epsilon^{i/2} \mu p_i\left(\tilde{R}, \tilde{Z}\right), \tag{A10}$$

where $\tilde{Z} \equiv \sqrt{\epsilon} z/a$ and $\tilde{R} \equiv R/a$ are dimensionless coordinates of order unity, and p_i, z_i and r_i are dimensionless functions, also of order unity. An important subtlety is the need to include a z_0 term in the expansion as, provided it does not depend upon R, it only generates an $\mathcal{O}(\sqrt{\epsilon})$ term in F. Indeed, comparing to the answer in the main text, we will later choose to write

$$z_{0,\tilde{Z}} = \frac{2^{7/12}}{\sqrt{3}} h\left(\tilde{Z}\right), \tag{A11}$$

where h is the function we are seeking, which varies between ± 1 over the domain wall.

Our strategy is to substitute these series expansions into the bulk equations (eqns A5 and A7) and boundary conditions (eqn A6), and solve at each successive order in ϵ to properly characterize the sympathetic strains that accompany z_0.

Both F and σ can also be expanded in ϵ,

$$F = \sum_{i=0}^{\infty} \epsilon^{i/2} F_i, \qquad \sigma = \sum_{i=0}^{\infty} \epsilon^{i/2} \sigma_i, \tag{A12}$$

and the zeroth terms in F and σ are

$$F_0 = \begin{pmatrix} 2^{-1/6} & 0 & 0 \\ 0 & 2^{-1/6} & 0 \\ 0 & 0 & 2^{1/3} \end{pmatrix} \tag{A13}$$

$$\frac{\sigma_0}{\mu} = \begin{pmatrix} 2^{-\frac{1}{6}} + 2^{\frac{1}{6}} P_0 & 0 & 0 \\ 0 & 2^{-\frac{1}{6}} + 2^{\frac{1}{6}} P_0 & 0 \\ 0 & 0 & 2^{\frac{1}{3}} + 2^{-\frac{1}{3}} P_0 \end{pmatrix}, \tag{A14}$$

which already solve eqns A5 and A7 (the bulk equations) to zeroth order. Inspecting the expansions for z and r, we see that $E_s = \Gamma a \mu 2\pi r z_{,Z} + \mathcal{O}(\epsilon^2)$, so the boundary conditions at $R = a$ can be written in much simpler form,

$$\sigma_{rR}/\mu = -\Gamma z_{,Z} + \mathcal{O}(\epsilon^{3/2}) \tag{A15}$$

$$\sigma_{zR}/\mu = \Gamma r_{,Z} + \mathcal{O}(\epsilon^{5/2}), \tag{A16}$$

and, to satisfy these to zeroth order, we require

$$P_0 = -\frac{9}{2^{1/3}}. \tag{A17}$$

To solve at $\mathcal{O}(\sqrt{\epsilon})$ we first need the next term in F,

$$F_1 = \begin{pmatrix} r_{1,\tilde{R}} & 0 & 0 \\ 0 & r_1/\tilde{R} & 0 \\ z_{1,\tilde{R}} & 0 & z_{0,\tilde{Z}} \end{pmatrix}. \tag{A18}$$

To satisfy the volume-conservation equation (eqn A7) at $\mathcal{O}(\sqrt{\epsilon})$ we require

$$2^{\frac{1}{6}} r_{1,\tilde{R}} + 2^{\frac{1}{6}} \frac{r_1}{\tilde{R}} + 2^{-\frac{1}{3}} z_{0,\tilde{Z}} = 0, \tag{A19}$$

and hence

$$r_1(\tilde{R}, \tilde{Z}) = -\frac{\tilde{R}}{2\sqrt{2}} z_{0,\tilde{Z}}, \tag{A20}$$

where we have set the complimentary function, $c(\tilde{Z})/\tilde{R}$, to zero as otherwise it diverges at the center of the cylinder. The next order in the stress is

$$\frac{\sigma_1}{\mu} = p_1 F_0^{-1} + \begin{pmatrix} -\frac{5}{\sqrt{2}} z_{0,\tilde{Z}} & 0 & \frac{9}{\sqrt{2}} z_{1,\tilde{R}} \\ 0 & -\frac{5}{\sqrt{2}} z_{0,\tilde{Z}} & 0 \\ z_{1,\tilde{R}} & 0 & \frac{11}{2} z_{0,\tilde{Z}} \end{pmatrix}.$$

Substituting this into the mechanical equilibrium equations (eqn A5), remembering that $\frac{\partial}{\partial Z} = \frac{\sqrt{\epsilon}}{a} \frac{\partial}{\partial \tilde{Z}}$ and $\frac{\partial}{\partial R} = \frac{1}{a} \frac{\partial}{\partial \tilde{R}}$, we see that at $\mathcal{O}(\sqrt{\epsilon})$, the first equation simplifies to $p_{1,\tilde{R}} = 0$, requiring

$$p_1(\tilde{R}, \tilde{Z}) = p_1(\tilde{Z}), \tag{A21}$$

while the second reduces to $z_{1,\tilde{R}\tilde{R}} + z_{1,\tilde{R}}/\tilde{R} = 0$, requiring

$$z_1(\tilde{R}, \tilde{Z}) = z_1(\tilde{Z}), \tag{A22}$$

where we have again set the complimentary function, $c(\tilde{Z}) \log(\tilde{R})$ to zero. Similarly, expanding the boundary conditions to $\mathcal{O}(\sqrt{\epsilon})$, eqn A16 is already satisfied, but eqn A15 is an algebraic equation for p_1 requiring

$$p_1(\tilde{Z}) = -\frac{3}{2^{2/3}} z_{0,\tilde{Z}}. \tag{A23}$$

To solve at $\mathcal{O}(\epsilon)$ we first need the next term in F,

$$F_2 = \begin{pmatrix} r_{2,\tilde{R}} & 0 & r_{1,\tilde{Z}} \\ 0 & r_2/\tilde{R} & 0 \\ z_{2,\tilde{R}} & 0 & z_{1,\tilde{Z}} \end{pmatrix}. \tag{A24}$$

To satisfy the volume-conservation equation (eqn A7) at $\mathcal{O}(\epsilon)$ we require

$$2^{\frac{1}{6}} r_{2,\tilde{R}} + 2^{\frac{1}{6}} \frac{r_2}{\tilde{R}} + 2^{-\frac{1}{3}} z_{1,\tilde{Z}} - \frac{3}{4 \times 2^{2/3}} z_{0,\tilde{Z}}^2 = 0, \tag{A25}$$

which is solved by

$$r_2(\tilde{R}, \tilde{Z}) = \frac{3\tilde{R}}{8 \times 2^{5/6}} z_{0,\tilde{Z}}^2 - \frac{\tilde{R}}{2\sqrt{2}} z_{1,\tilde{Z}}. \tag{A26}$$

The next term in σ then simplifies to

$$\frac{\sigma_2}{\mu} = p_2 F_0^{-1} + \begin{pmatrix} -5 z_{1,\tilde{Z}}/\sqrt{2} & 0 & ... \\ 0 & -5 z_{1\tilde{Z}}/\sqrt{2} & 0 \\ z_{2,\tilde{R}} - \frac{9}{4} \tilde{R} z_{0,\tilde{Z}\tilde{Z}} & 0 & ... \end{pmatrix},$$

where we have not displayed the rZ and zZ entries since they do not enter the equations at $\mathcal{O}(\epsilon)$. Expanding the mechanical equilibrium equations (eqn A5) to $\mathcal{O}(\epsilon)$, first equation simplifies to $p_{2,\tilde{R}} = 0$, requiring

$$p_2(\tilde{R}, \tilde{Z}) = p_2(\tilde{Z}), \tag{A27}$$

and the second simplifies to

$$z_{2,\tilde{R}\tilde{R}} - \frac{9}{4} z_{0,\tilde{Z}\tilde{Z}} + \frac{11}{2} z_{0,\tilde{Z}\tilde{Z}} - \frac{3}{2} z_{0,\tilde{Z}\tilde{Z}} + \frac{z_{2,\tilde{R}}}{\tilde{R}} - \frac{9}{4} z_{0,\tilde{Z}\tilde{Z}} = 0, \tag{A28}$$

which we can solve to find

$$z_2(\tilde{R}, \tilde{Z}) = C(\tilde{Z}) + \frac{1}{8} \tilde{R}^2 z_{0,\tilde{Z}\tilde{Z}}. \tag{A29}$$

Expanding out the boundary conditions to $\mathcal{O}(\epsilon)$, eqn A15 is an algebraic equation for p_2 that requires

$$p_2(\tilde{Z}) = -2^{1/6} - \frac{3}{2^{2/3}} z_{1,\tilde{Z}}, \tag{A30}$$

while eqn A16 is already satisfied.

Recalling from the main text that instability occurs when the tension is,

$$T = \frac{\pi\mu a^2}{2^{2/3}}\left(9+\sqrt{2}\epsilon+\mathcal{O}(\epsilon^2)\right), \tag{A31}$$

and writing

$$z_{0,\tilde{Z}} = \frac{2^{7/12}}{\sqrt{3}} h\left(\tilde{Z}\right), \tag{A32}$$

we can now expand out the total energy per unit length (eqn A2) to $\mathcal{O}(\epsilon^2)$, to get

$$\frac{\mathcal{E}}{\pi\mu a^2} = \frac{9}{\sqrt[3]{2}} + 2^{\frac{1}{6}}\pi a^2\mu\epsilon + \left(\frac{25h''}{16\sqrt[12]{2}\sqrt{3}} + c_1\right)\epsilon^{3/2} + \frac{1}{12\sqrt[3]{2}}\left(h^2\left(h^2-2\right) - 2\sqrt{2}hh'' + \frac{17}{4\sqrt{2}}h'^2 + c_2\right)\epsilon^2 + \mathcal{O}(\epsilon^{5/2}), \tag{A33}$$

where c_1 and c_2 are quite complicated expressions involving higher order fields, but do not contain any h dependence. The above expression is the exact version of the approximate eqn 13 in the main text. We note that one would naively expect cross terms between z_0 (which generates $\mathcal{O}(\sqrt{\epsilon})$ stress/strains) and the z_3, r_3, p_3 fields (which generate $\mathcal{O}(\epsilon^{3/2})$ stress/strains) at $\mathcal{O}(\epsilon^2)$ in $\mathcal{E}$, but upon actually doing the expansion, we find these terms vanish identically; such cancelation is actually expected since the coefficient of such cross-terms would be the curvature (second derivative) of the energy at $\epsilon = 0$, which is zero since we are expanding about the point of instability. Minimizing with respect to variations in h, the $\mathcal{O}(\epsilon^{3/2})$ term is an exact derivative, so it does not contribute, but minimizing the $\mathcal{O}(\epsilon^2)$ term gives:

$$4h\left(h^2-1\right) = \frac{33}{2\sqrt{2}}h'', \tag{A34}$$

which is solved by the domain wall taking the form

$$h(\tilde{Z}) = \tanh\left(\frac{2^{5/4}\tilde{Z}}{\sqrt{33}}\right)$$
$$\implies h(Z) = \tanh\left(\frac{2^{5/4}\sqrt{\epsilon}}{\sqrt{33}a}Z\right). \tag{A35}$$

This is almost identical to the approximate result in the main text, but with a characteristic width for the domain wall smaller by a factor of $\sqrt{34/33}$.

Appendix B: Details of numerical simulations

Our simulations use an explicit finite-element method, based on the same code used in [43, 44], with the additions of surface tension and cylindrical symmetry as first implemented in [15]. More precisely, we construct the elastic cylinder from constant-strain triangular elements in the $r-z$ plane, each of which represents a triangularly cross-sectioned torus of the body. The triangles form a rectangular mesh in the $r-z$ plane, spanning from $r=0$ (the center of the cylinder) to an outer radius of $r=a$, and from $z=0$ to $z=L/2$, and we enforce symmetric boundary conditions at the two ends ($z=0, L/2$), so that our simulation domain need only contain a half-wavelength of the instability, as show below in fig. 5.

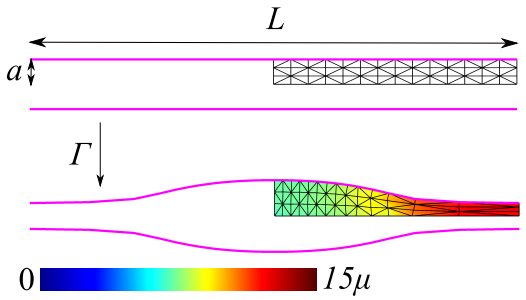

FIG. 5. Top: The actual simulation mesh is a triangulated rectangular mesh between $0 < r < a$ and $0 < z < L/2$, which covers only 1/4 of the total cylinder. For visualization purposes, the mesh shown here has only 15×4 nodes, and hence 84 triangles, which is many fewer than those used in the paper. Bottom: The same mesh at equilibrium after a surface tension $\Gamma = 9$ has been applied. Color indicates pressure.

The simulation images in the paper do not show the entire fine mesh, but do have white lines indicating every 8th mesh line in the length direction. Each triangle in the mesh is assigned a compressible neo-Hookean elastic energy (within a quasi-incompressible nodal pressure formulation) with shear modulus μ with a bulk modulus $K \geq 10^3\mu$. The force on each node is calculated as the gradient of the total energy with respect to nodal position, including surface energy at the outer surface, and the nodes are moved according to damped Newtonian dynamics. The calculations required us to either change Γ (fig 1, 3b and 4b) at constant overall stretch (λ), or change the overall stretch at constant Γ (fig 3c and 4a), but in each calculation the changes were imposed slowly enough as to be quasi-static, so although the simulation uses Newtonian dynamics, the states reported in the paper are all converged energy minima. The good agreement between the predicted and observed thresholds and amplitude verify that the the bulk modulus was high enough, the mesh was fine enough and the simulations were slow enough to mimic an incompressible, equilibrated continuum cylinder.

We summarize the exact simulation parameters for each figure in the table below.

Figure	Γ	L/a	λ	K/μ	Mesh
1	5,6,7,9	100	1	10^3	400×8
3b	5.7	200	1.2	10^4	800×8
and	$5.7 - 6$	100	1.2	10^4	400×8
4b-c	> 6	100	2	10^4	400×8
3c and 4a	10	200	0.214 - 5	10^3	800×8
Movie S1	8	100	1	10^3	400×8
Movie S2	8	50	0.25-4	10^3	200×8

In the calculations at fixed λ (fig 1, 3b, 4b-c) the surface tension was set to the desired value at the outset, and in the first few simulation steps the boundaries were moved to impose the desired λ. The cylinder was then held fixed, and instability naturally set in at finite wavelength, coarsening over time, but increasingly slowly as the wavelength increased, as might be expected since the domain walls are exponentially localized. To speed the calculation up, in most calculations the coarsening was accelerated by an early-time perturbation wherein the surface tension changed along the cylinder from $\Gamma + 1$ at one end to Γ at the other. The results shown are all states from long after this perturbation has been removed, and the system has converged. We note that movie S1 verifies that the coarsening does achieve the longest possible wavelength unaided eventually, and that a long wavelength would naturally be selected if Γ was increased slowly from the stable to the unstable regime, rather than simply being set to its desired final value. In the calculations with varying λ (fig 3c, 4a and Movie S2) the cylinder naturally and quickly selected the long-wavelength mode at the point of instability, so no acceleration was necessary.

[1] B. Roman and J. Bico, Journal of Physics: Condensed Matter **22**, 493101 (2010).
[2] J. Van Honschoten, M. Escalante, N. Tas, and M. Elwenspoek, Journal of colloid and interface science **329**, 133 (2009).
[3] W. Zuo, M. Zhu, W. Yang, H. Yu, Y. Chen, and Y. Zhang, Polymer Engineering & Science **45**, 704 (2005).
[4] M. Naraghi, I. Chasiotis, H. Kahn, Y. Wen, and Y. Dzenis, Applied Physics Letters **91** (2007).
[5] A. L. Hazel and M. Heil, Proceedings of the Royal Society A: Mathematical, Physical and Engineering Science **461**, 1847 (2005).
[6] E. Hannezo, J. Prost, and J.-F. Joanny, Physical Review Letters **107**, 078104 (2011).
[7] J. Dervaux, Y. Couder, M.-A. Guedeau-Boudeville, and M. Ben Amar, Physical review letters **107**, 018103 (2011).
[8] D. Gonzalez-Rodriguez, S. Sart, A. Babataheri, D. Tareste, A. I. Barakat, C. Clanet, and J. Husson, Phys. Rev. Lett. **115**, 088102 (2015).
[9] E. S. Matsuo and T. Tanaka, Nature **358**, 482 (1992).
[10] B. Barriere, K. Sekimoto, and L. Leibler, The Journal of chemical physics **105**, 1735 (1996).
[11] S. Mora, T. Phou, J.-M. Fromental, L. M. Pismen, and Y. Pomeau, Phys. Rev. Lett. **105**, 214301 (2010).
[12] P. Ciarletta and M. Ben Amar, Soft Matter **8**, 1760 (2012).
[13] M. Taffetani and P. Ciarletta, Journal of the Mechanics and Physics of Solids (2015).
[14] M. Taffetani and P. Ciarletta, Phys. Rev. E **91**, 032413 (2015).
[15] C. Xuan and J. Biggins, Physical Review E **94**, 023107 (2016).
[16] C. Py, P. Reverdy, L. Doppler, J. Bico, B. Roman, and C. N. Baroud, Phys. Rev. Lett. **98**, 156103 (2007).
[17] J. Bico, B. Roman, L. Moulin, and A. Boudaoud, Nature **432**, 690 (2004).
[18] H.-Y. Kim and L. Mahadevan, Journal of Fluid mechanics **548**, 141 (2006).
[19] S. Mora, C. Maurini, T. Phou, J.-M. Fromental, B. Audoly, and Y. Pomeau, Phys. Rev. Lett. **111**, 114301 (2013).
[20] R. W. Style, R. Boltyanskiy, Y. Che, J. Wettlaufer, L. A. Wilen, and E. R. Dufresne, Phys. Rev. Lett. **110**, 066103 (2013).
[21] R. W. Style, C. Hyland, R. Boltyanskiy, J. S. Wettlaufer, and E. R. Dufresne, Nature Com. **4** (2013).
[22] R. W. Style, Y. Che, S. J. Park, B. M. Weon, J. H. Je, C. Hyland, G. K. German, M. P. Power, L. A. Wilen, J. S. Wettlaufer, *et al.*, Proc. of the Nat. Acad of Sci. **110**, 12541 (2013).
[23] M. B. Amar and P. Ciarletta, Journal of the Mechanics and Physics of Solids **58**, 935 (2010).
[24] J. Yoon, J. Kim, and R. C. Hayward, Soft Matter **6**, 5807 (2010).
[25] S. Mora, M. Abkarian, H. Tabuteau, and Y. Pomeau, Soft Matter **7**, 10612 (2011).
[26] A. Gent, Rubber Chemistry and Technology **63**, 49 (1990).
[27] J. Strutt (Lord Rayleigh), "On the instability of jets," (1879).
[28] P. P. Bhat, S. Appathurai, M. T. Harris, M. Pasquali, G. H. McKinley, and O. A. Basaran, Nature Physics **6**, 625 (2010).
[29] J. Eggers, Rev. Mod. Phys. **69**, 865 (1997).
[30] J. Clerk-Maxwell, Nature **11**, 357 (1875).
[31] V. S. Markin, D. L. Tanelian, R. A. Jersild, and S. Ochs, Biophysical journal **76**, 2852 (1999).
[32] S. S. Antman, Journal of Mathematical Analysis and Applications **44**, 333 (1973).
[33] J. Ericksen, Journal of elasticity **5**, 191 (1975).
[34] A. Gent, Rubber chemistry and technology **72**, 263 (1999).
[35] F. Meng, J. Z. Chen, Z. Ouyang, *et al.*, AIChE Journal **60**, 1393 (2014).
[36] T. Tanaka, Phys. Rev. Lett. **40**, 820 (1978).
[37] A. Boudaoud and S. Chaïeb, Phys. Rev. E **68**, 021801 (2003).
[38] M. Mooney, Journal of applied physics **11**, 582 (1940).
[39] R. Rivlin, Philosophical Transactions of the Royal Society of London A: Mathematical, Physical and Engineering Sciences **241**, 379 (1948).

[40] A. Gent, Rubber chemistry and technology **69**, 59 (1996).
[41] E. M. Arruda and M. C. Boyce, Journal of the Mechanics and Physics of Solids **41**, 389 (1993).
[42] S. Poliak and E. Peles, Nature Reviews Neuroscience **4**, 968 (2003).
[43] T. Tallinen, J. Y. Chung, J. S. Biggins, and L. Mahadevan, Proceedings of the National Academy of Sciences **111**, 12667 (2014).
[44] T. Tallinen and J. S. Biggins, Phys. Rev. E **92**, 022720 (2015).